# Exciton and exciton-magnon photoluminescence in the antiferromagnet CuB$_2$O$_4$

D. Kudlacik [●],[1] V. Yu. Ivanov [●],[2] D. R. Yakovlev [●],[1,3] V. F. Sapega [●],[3] J. J. Schindler [●],[1] J. Debus [●],[1]
M. Bayer [●],[1,3] and R. V. Pisarev [●][3]

[1]*Experimentelle Physik 2, Technische Universität Dortmund, 44221 Dortmund, Germany*
[2]*Institute of Physics Polish Academy of Sciences, PL-02-668 Warsaw, Poland*
[3]*Ioffe Institute, Russian Academy of Sciences, 194021 St. Petersburg, Russia*

Copper metaborate CuB$_2$O$_4$ crystallizes in a unique noncentrosymmetric structure, becomes antiferromagnetically ordered below $T_{N1} = 20$ K, and exhibits a great diversity in magnetic, optical, and magneto-optical properties. In particular, it shows strong photoluminescence rarely observed before in other magnetically ordered copper oxides in which magnetic properties are defined by magnetic Cu$^{2+}$ ($3d^9$, $S = 1/2$) ions. Here we report on the detailed spectroscopic study of the photoluminescence originating from the Cu$^{2+}$ ions. Our investigations are focused on understanding the energy-level scheme of the multiple excitations below the energetically lowest, crystal-field-split $d$-$d$ electronic transition at 1.405 eV. We identify multiple emission lines, and among them we distinguish three sets of lines, each composed of an exciton line and a satellite attributed to magnon-assisted exciton recombination. The emission intensity of the three sets changes strongly in the temperature range 1.7–40 K, showing pronounced correlations with the magnetic phase transitions between the commensurate and incommensurate phases. Photoluminescence excitation spectra and time-resolved emission dynamics give closer insight into the energy relaxation channels populating the exciton-magnon sets.

## I. INTRODUCTION

Multiferroic and magnetoelectric materials are characterized by mutual interactions between magnetic, electric, and lattice subsystems, leading to the observation of intriguing physical phenomena with promising potential for developing new technologies [1–7]. Along with the studies of their magnetic, electric, dielectric, and other properties, over the last decades significant efforts have been devoted to investigating linear and nonlinear optical and magneto-optical effects in multiferroics and magnetoelectrics. Due to the simultaneous breaking of space inversion and time reversal symmetries, new types of interactions between the electronic, spin, and orbital degrees of freedom leading to new optical phenomena have been highlighted [8–16]. While some of these effects have been successfully explored, others are still waiting for further studies and unambiguous explanations, in particular, on the microscopic scale.

Among the various types of multiferroics, the magnetoelectric antiferromagnet copper metaborate CuB$_2$O$_4$ is a particularly prominent example. It possesses a unique noncentrosymmetric crystal structure and a complex magnetic phase diagram; see the most recent publications [17,18] and references therein. Many interesting effects were observed in the studies of linear and nonlinear optical properties. First measurements of optical absorption and second harmonic generation demonstrated an exceptionally rich exciton and exciton-phonon sideband spectra [19,20]. Detailed analysis of the absorption spectra allowed evaluation of the whole set of genuine crystal field parameters [21]. Lattice dynamics of CuB$_2$O$_4$ were explored by means of polarized infrared and Raman spectroscopy to make a reliable identification of all Brillouin-zone-center phonons and two-magnon excitation modes [22,23].

Several other experimental techniques were applied for investigating CuB$_2$O$_4$. Resonant inelastic x-ray scattering was applied for the studies of the well-isolated low-energy features [24]. It was concluded that they should be attributed to the $d$-$d$ transitions rather than to the charge-transfer excitation discussed in other copper oxides. The local electronic structure of copper ions in CuB$_2$O$_4$ was studied by using polarization-dependent x-ray absorption spectroscopy where theoretical calculations were used for separating the contributions of the two nonequivalent positions of the copper ions in the unit cell of CuB$_2$O$_4$ to the absorption and x-ray circular dichroism spectra [25].

In CuB$_2$O$_4$ below the Néel temperature $T_{N1} = 20$ K, spatial inversion and time reversal symmetry are both broken, opening up new appealing possibilities for the investigation of various optical effects. For instance, a strong change of the optical absorption with reversal of the light propagation direction [12], as well as a directional asymmetry in the photoluminescence spectra were reported [26]. Here it is worth noting that some optical effects observed in this complicated material have raised conflicting discussions regarding their physical origin. One of the disputed topics was the magnetic field control of the crystal chirality reported in Ref. [27], which was later found to be inconsistent with the theoretical analysis of the dichroic signals from CuB$_2$O$_4$ [28]. As far as we know, this issue has not been resolved so far [29–31]. Recent studies of CuB$_2$O$_4$ dealt with the femtosecond activation of magnetoelectricity [32], the excitation of coherent phonons [33], the microwave induced magneto-chiral effect [34], and besides the optical effects, the observation of complex behavior of thermal conductivity with well-pronounced anomalies at several magnetic phase transitions [18].

035128-1

The photoluminescence (PL) technique is widely and efficiently used for characterization of the optical and electronic properties of solids as well as for investigation of spin related phenomena [35,36]. Technically, it can be accomplished quite easily by excitation of the material under study with photons, either from a lamp or a laser, with energy typically well above the one where the PL occurs, and analyzing spectrally the light emitted by radiative recombination of the electronic excitations. However, the occurrence of PL is not self-evident as it requires optically allowed transitions with finite quantum efficiency. For magnetically ordered dielectrics PL has remained a very rare phenomenon. So far, it has been assumed that the quenching of radiative recombination in these materials originates from strong interactions between the magnetic ions, electron-phonon and spin-lattice coupling. The reported experimental data allow one to assume that the PL is more pronounced in the ionic dielectric crystals, e.g., in the $3d^n$ fluorides, in comparison to covalent dielectrics such as the $3d^n$ oxides. Therefore, recent observations of bright PL from the magnetic oxide on the basis of $Cu^{2+}$ ions in the antiferromagnetic dielectric $CuB_2O_4$ were a big surprise [26,37–39]. To the best of our knowledge, no other reports are available on PL from magnetically ordered materials associated with the Jahn-Teller $Cu^{2+}$ ions so far. These observations open up new opportunities for the studies of electronic structure, magnetic phase transitions, and other properties of $CuB_2O_4$. Moreover, time-resolved PL spectroscopy allows one to study the relaxation dynamics of the different excited electronic states. So $CuB_2O_4$ is a very suitable sample allowing one to leverage these potentialities.

In this paper, we report a detailed PL study of $CuB_2O_4$, including its recombination dynamics, conducted in a temperature range from 1.7 K up to well above $T_{N1} = 20$ K, where several magnetic phase transitions occur. We put the emphasis on the origin of the emission lines and determine the energy-level scheme of the multiple excitations of $Cu^{2+}$ ions below the energetically lowest crystal-field-split $d$-$d$ transition, located at the photon energy of 1.4052 eV. We identify three sets of emission lines, each composed of an exciton line and a satellite attributed to magnon-assisted exciton recombination.

The paper is organized as follows: In Secs. II A–II C, we briefly overview the crystal structure, the magnetic and the optical properties of $CuB_2O_4$. In Sec. II D we consider the specifics of the strongly bound Frenkel excitons in magnetically ordered materials resulting in magnon-assisted exciton recombination. The samples and experimental techniques are described in Sec. III. The experimental results are collected and discussed in Sec. IV. In Sec. V we summarize our conclusions and present a scheme of the electronic levels contributing to PL.

## II. COPPER METABORATE CuB₂O₄

### A. Crystal structure

The dielectric oxide $CuB_2O_4$ crystallizes in the tetragonal noncentrosymmetric space group $I\bar{4}2d$ (no. 122) comprising a large primitive unit cell with 42 atoms [40,41]. The lattice constants are $a = b = 1.1528$ nm and $c = 0.5607$ nm [40]. Temperature variations of the lattice parameters were reported
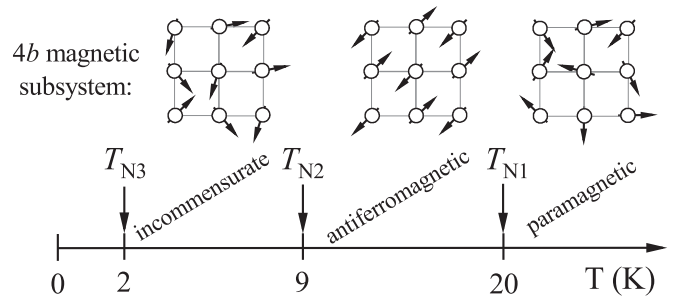


FIG. 1. Schematic magnetic phase diagram at $B = 0$ T of the $4b$ subsystem in $CuB_2O_4$. At the temperatures $T_{N1}$, $T_{N2}$, and $T_{N3}$, the $Cu^{2+}$ ions in the $4b$ sites undergo different types of phase transitions at which their spin configuration changes. Starting from high temperatures, the magnetic structure evolves from the paramagnetic phase above 20 K to an antiferromagnetic phase below 20 K and further, to an incommensurate phase below 9 K. The exact magnetic structure below the phase transition at 2 K is not known.

in Ref. [42]. The optical $c$ axis is oriented along the [001] crystallographic direction ($c \parallel z \parallel$ [001]). The basal plane is perpendicular to the [001] direction and is formed by the two equivalent $a$ and $b$ axes ($a \parallel x \parallel$ [100] and $b \parallel y \parallel$ [010]). The structure is characterized by 12 Jahn-Teller $Cu^{2+}$ ($3d^9$) ions occupying the two nonequivalent $4b$ and $8d$ crystallographic positions. While on the $8d$ sites each $Cu^{2+}$ ion is surrounded by six $O^{2-}$ ions forming a strongly elongated oxygen octahedron (site symmetry 2), on the $4b$ sites each $Cu^{2+}$ ion has only four nearest $O^{2-}$ ions in a planar configuration (site symmetry $-4$). Due to this exceptional configuration of the Jahn-Teller $Cu^{2+}$ ions on both crystallographic positions, the structure of $CuB_2O_4$ seems to be unique among multiferroic and magnetoelectric materials. The only known exception of a similar crystal structure is $PdB_2O_4$ with the $Pd^{2+}$ ($4d^8$) magnetic ions [43]. However, to the best of our knowledge, no information on its magnetic and optical properties is available.

### B. Magnetic structure and phase transitions

The interlaced $4b$ and $8d$ subsystems of the magnetic $Cu^{2+}$ ($S = 1/2$) ions are coupled by intra- and intersubsystem exchange interactions resulting in intricate commensurate and incommensurate magnetic structures; see Ref. [17] and references therein. These magnetic structures and the transitions between them depend on temperature as well as an applied magnetic field strength and direction with respect to the crystallographic axes. The magnetic phase diagrams differ significantly for magnetic fields applied parallel to the $c$ axis ($\mathbf{B} \parallel c \parallel$ [001]) or in the basal plane ($\mathbf{B} \perp$ [001]). These diagrams have been studied in several publications [10,44–51]; however, the given parameters slightly deviate from each other. The most recent comprehensive information, to which we will refer here, can be found in Ref. [17].

The phase transitions of the magnetic $4b$ subsystem at zero magnetic field are schematically shown in Fig. 1. With decreasing temperature, the structure undergoes at the Néel temperature $T_{N1} = 20$ K the first phase transition from the paramagnetic to the antiferromagnetic phase due to the exchange interactions within the $4b$ subsystem [17]. A further

temperature decrease results to the another phase transition into an incommensurate phase at $T_{N2} = 9$ K. It is provided by the exchange interaction between the $4b$ and $8d$ subsystems and results in partial ordering of the $8d$ subsystem [17,44,52]. Finally, the $Cu^{2+}$ magnetic moments reorient at $T_{N3} \approx 2$ K forming a new state [17,44–46]. In fact, this is a simplified consideration, which will be sufficient for understanding the modifications of the optical spectra reported in this paper. The magnetic properties of $CuB_2O_4$ are rich, including several magnetic phases and transitions between them, especially in an external magnetic field but they will not be discussed here. The origin of these phase transitions is not fully understood so far.

### C. Optical properties

The particular local symmetry of the $Cu^{2+}$ ions ($3d^9$ shell, $S = 1/2$, $L = 0$) in the two crystallographic positions leads to the nontrivial electronic structure of $CuB_2O_4$ [20]. Its optical absorption spectrum shows six zero-phonon (ZP) lines, whose polarization properties are mostly in accordance with the electric-dipole (ED) selection rules [21]. The symmetry analysis and their polarization properties allow us to assign these ZP lines to Frenkel exciton states on the photoexcited $Cu^{2+}$ ions. A detailed group theory consideration shows that excitons at the $\Gamma$ point can be excited either via ED or magnetic-dipole (MD) processes [53]. The lowest exciton state at 1.4052 eV belongs to the $4b$ subsystem and the next one at 1.5767 eV is associated with the $8d$ subsystem. Above the exciton lines the absorption spectrum has a rich fine structure formed mostly by phonon sidebands. The phonon spectrum in $CuB_2O_4$ has been studied by infrared Fourier spectroscopy and Raman scattering [22,23].

The absorption spectra of $CuB_2O_4$ are strongly sensitive to the orientation of the linear polarization plane of the exciting light and the direction of its wave vector **k** with respect to the crystallographic axes. Experiments performed at $T = 5$ K, which are presented in Ref. [21], highlight that in the spectral range from 1.405 to 1.576 eV absorption is observed in geometries where the electric field vector of light **E** is perpendicular to the $c$ axis, i.e., either for the $\alpha$ spectrum (**k** $\parallel$ $c$, **E** $\perp$ $c$) or the $\sigma$ spectrum (**k** $\perp$ $c$, **E** $\perp$ $c$). The absorption in this region is nearly absent in the $\pi$ spectrum (**k** $\perp$ $c$, **E** $\parallel$ $c$).

Very bright photoluminescence at low temperatures has been found in the spectral range below the first $d$-$d$ electronic transition at 1.4052 eV, so that it is associated with the $Cu^{2+}$ ions in the $4b$ subsystem [26,37–39]. It shows a very rich structure of narrow and broader spectral lines and extends down to 1.2 eV. We will show that the PL spectrum originates from emission of Frenkel exciton ZP lines and lines assisted by phonon and magnon generation. The involvement of impurity and trap states in the emission process is also highly probable. At present, a reliable identification of the PL lines is missing. Hence, our goal is to take the first steps in this direction: we focus here on the identification of the exciton and magnon-assisted exciton recombination lines in the emission, demonstrating their strong sensitivity to the magnetic phase prevailing for the particular experimental conditions.
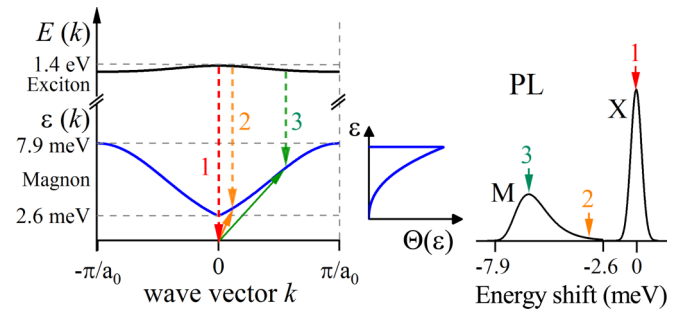


FIG. 2. (Left) Scheme of the exciton [$E(k)$] and magnon [$\varepsilon(k)$] dispersions. Small insert to the right displays the magnon density of states [$\Theta(\varepsilon)$] as a function of the energy ($\varepsilon$). Optical transitions are shown by dashed arrows: (1) zero-phonon and zero-magnon exciton recombination, (2) exciton-magnon assisted process in the center of the Brillouin zone, $K = -k_m \geqslant 0$, (3) exciton-magnon assisted process with $K = -k_m \leqslant \pi/a_0$. (Right) Scheme of the emission spectrum contributed by the exciton (X) and magnon-assisted exciton (M) recombination where zero energy corresponds to the zero-phonon transition. The given low-energy shifts are characteristic for magnons in $CuB_2O_4$ [61,62].

### D. Exciton and exciton-magnon emission in antiferromagnets

In typical antiferromagnetic crystals, such as $MnF_2$, $FeF_2$, $RbMnF_3$, $CoF_2$, *et al.*, particular optical features attributed to exciton and exciton-magnon transitions in the near infrared, visible and ultraviolet spectral ranges were reported [54–57]. They are related to electronic excitations within a $3d^n$ magnetic ion, resulting in formation of a Frenkel exciton of small radius, which in turn may interact with magnons [58]. The theoretical approach for describing the exciton and exciton-magnon states in magnetically ordered crystals and their contribution to the absorption and emission spectra was developed in several publications; see, e.g., Refs. [57,59,60].

With regard to the pure electronic transitions, as consequence of the electric-dipole (ED) approximation, exciton recombination is parity forbidden for ions with a partially filled $3d^n$ electron configuration. Most of exciton observations were made in centrosymmetric crystals, e.g., in the antiferromagnets $MnF_2$ and $RbMnF_3$ [54–56]. Here the exciton absorption line has polarization properties compatible with an allowed MD transition, while the magnon-assisted sidebands are polarized as expected for an ED transition due to the specific magnon-assisted ED mechanism, which lifts the restrictions on the parity-forbidden process [59].

Model considerations and schemes for exciton and magnon-assisted exciton absorption in a $MnF_2$ antiferromagnetic crystal can be found in Ref. [58]. Since we investigate emission spectra in our paper, we need to modify this consideration for photoluminescence. The respective scheme is given in Fig. 2 including the characteristic energies for the excitons and magnons associated with the $Cu^{2+}$ ions in $CuB_2O_4$. The exciton and magnon dispersions are shown on the left side. The exciton band is indicated almost as a straight line, as it has a much smaller dispersion than the magnons. The optical transitions with emission of photons with **k** $\approx 0$ obey the momentum conservation law. For exciton recombination without additional phonon or magnon involvement, the

resulting selection rule simply is $\mathbf{K} = \mathbf{k} \approx 0$, where $\mathbf{K}$ is the exciton wave vector. This optical transition is shown by the arrow 1 in Fig. 2 and leads to a narrow exciton emission line.

In the case of the magnon-assisted exciton recombination, momentum and energy is shuffled into the system of magnetic ions in form of magnons with momentum $\mathbf{k}_m$. The momentum conservation law $\mathbf{K} - \mathbf{k}_m = \mathbf{k} \approx 0$ leads to a low-energy shift of the magnon-assisted exciton recombination line from the zero-phonon exciton emission line given by the magnon energy. While magnons in the center of the Brillouin zone $\mathbf{k}_m \approx 0$ (optical transition 2 in Fig. 2) have an energy of about 2.6 meV, magnons at the edge of the Brilloiun zone have 7.9 meV energy. Here we use the magnon dispersion parameters measured for $CuB_2O_4$ at $T = 2$ K [61,62]. As a result the exciton-magnon emission forms a band that is extended over 5.3 meV, and its shape is determined by the exciton and magnon dispersions, the transition matrix element, temperature, and other factors. It has an asymmetric shape, as schematically shown in Fig. 2.

## III. SAMPLE AND EXPERIMENTAL METHODS

We studied single crystals of $CuB_2O_4$ grown by the Kyropoulos technique from a melt of $B_2O_3$, CuO, $Li_2O$, and $MoO_3$ oxides [63]. For this study, a plane-parallel polished (010)-plate with the thickness of 1.12 mm was cut out of the single crystal and oriented using Laue x-ray diffraction patterns. The crystallographic $c$ axis ($c \parallel [001]$) called the optical axis of a uniaxial crystal was in the plane of the sample. In the experiments reported here the wave vectors of the excitation laser and of the emitted photons were always perpendicular to the c axis ($\mathbf{k} \perp c$); see Fig. 3(a).

The sample was mounted strain-free in a split-coil magnet cryostat, which allowed us to perform optical measurements in the temperature range from 1.7 up to 300 K. The temperature was monitored with a sensor mounted in the sample vicinity. In the absorption measurements, a laser-driven plasma white lamp was used as exciting light source. For excitation of the PL a continuous-wave Ti:sapphire laser tunable in the range from 1.3 up to 1.5 eV was applied. The laser light was linearly polarized and its polarization was kept perpendicular to the $c$ axis ($\mathbf{E} \perp c$) to optimally match the best absorption conditions of the crystal-field-split $d$-$d$ transition in the 4$b$ subsystem [21]. The power density at the sample surface was typically set to about $P_{exc} = 1$ mW/cm$^2$, unless specified otherwise. The laser power was stabilized by a liquid-crystal variable attenuator. For most PL measurements presented here nonresonant excitation with the photon energy of $E_{exc} = 1.42$ eV was used. PL excitation (PLE) spectra were measured by detecting emission of specific emission lines while tuning the laser photon energy. The transmitted light (absorption measurement) or the PL were spectrally resolved by a 1-meter double monochromator (Model U1000, Jobin-Yvon) equipped with a liquid nitrogen cooled charge-coupled device (CCD) detector. The double additive mode of the monochromator provides a spectral resolution of 0.1 meV and a high stray light rejection. To be able to resolve all features in the PL and PLE spectra with sufficient resolution, the measurement time per spectrum with the CCD was 4 min.
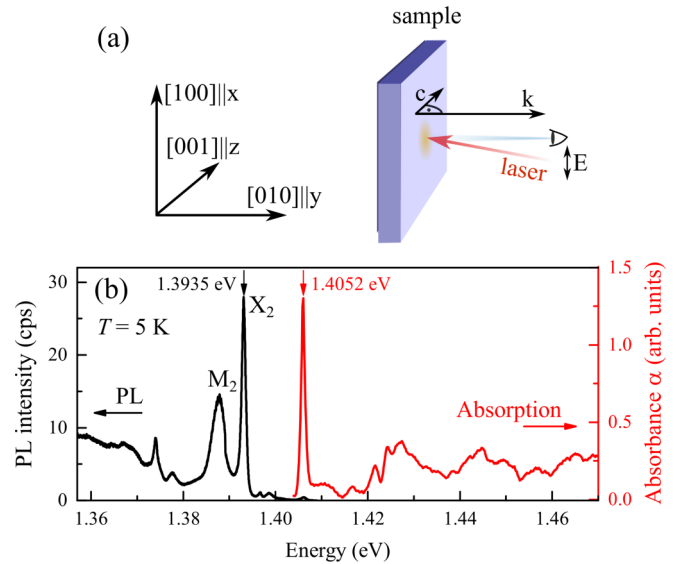


FIG. 3. (a) Sample orientation and experimental geometry. (b) Photoluminescence spectrum (black line) and $\sigma$ absorption spectrum (red line, $\mathbf{k} \perp c$, $\mathbf{E} \perp c$) of $CuB_2O_4$ in the energy range of the lowest-in-energy $d$-$d$ transition of the 4$b$ subsystem. $T = 5$ K, $E_{exc} = 1.45$ eV. Arrows and numbers indicate the position of the ZP line in absorption (a transition between the ground ($x^2 - y^2$) state and the first ($xy$) excited state) and the exciton transition ($X_2$) in luminescence.

In order to ensure a stable detection position on the sample surface, the sample was covered by a mask containing a hole of 500 $\mu$m diameter. The laser spot diameter on the sample surface was 250 $\mu$m. The central part of $100 \times 100$ $\mu$m$^2$ of this spot was selected by a cross slit positioned in the intermediate focus of the detection optical scheme.

In the time-resolved PL measurements we used a laser system generating 5-ns pulses with a repetition rate of 0.1 Hz. The laser wavelength was 532 nm ($E_{exc} = 2.33$ eV). Unless specified otherwise, the total average power of the laser was set to about $P_{exc} = 1$ mW/cm$^2$ at the sample surface. The PL was detected by a 1.5-m triple monochromator equipped with a gated CCD detector having a time resolution of 1 ns. We investigated two time ranges more closely. On the one hand the sub-$\mu$s range, which provides information about fast carrier recombination processes and population times, and on the other hand the ms range, which was used to analyze the long carrier recombination times of up to 250 $\mu$s. To resolve effects in the $\mu$s range, we used a measurement window of 0 to 30 $\mu$s with a measurement time per PL spectrum of 100 ns and 30 000 repetitions. The step between two measurements was 0.2 $\mu$s. For the investigation of the ms range the measurement window was increased to 1 ms and the measurement time per PL spectrum was increased to 1 $\mu$s. Here the step between two measurements was 2 $\mu$s.

## IV. EXPERIMENTAL RESULTS

### A. Temperature dependence of photoluminescence

Absorption and PL spectra of $CuB_2O_4$ measured at $T = 5$ K are shown in Fig. 3(b). The absorption spectrum, which
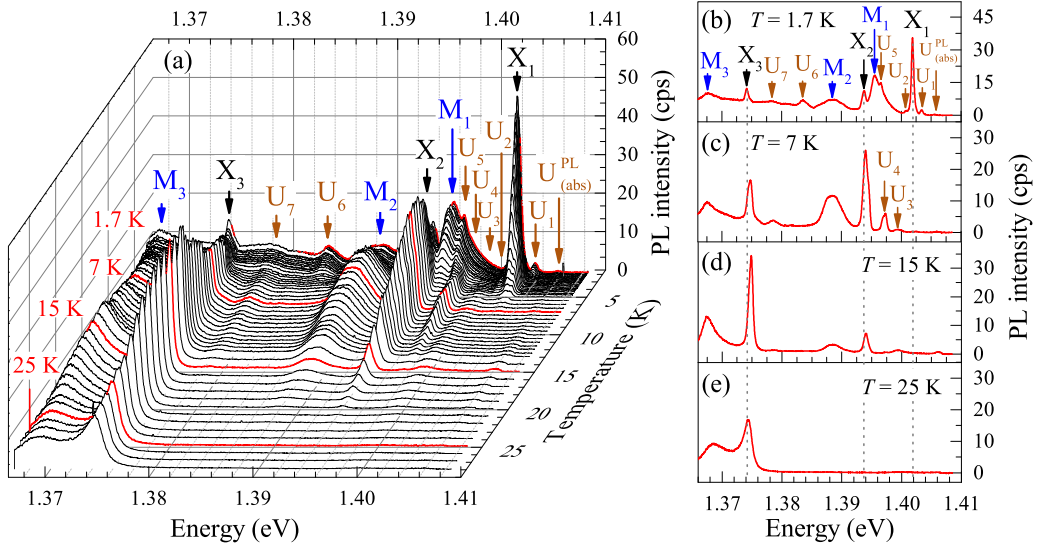
FIG. 4. (a) PL spectra at various temperatures measured for nonresonant excitation at $E_{exc} = 1.42$ eV using $P_{exc} = 1$ mW/cm$^2$. All lines are labeled and marked by the vertical arrows. The red PL spectra in panel (a) are shown in panels (b)–(e) for better comparison.

in general shows features in a wide energy range from 1.35 to 2.5 eV [21], is shown here only in the low-energy range. It has a sharp, intense line at 1.4052 eV accompanied at high-energy side by a rich phonon sideband structure. The line corresponds to the ZP exciton absorption and originates from the lowest-in-energy $d$-$d$ exciton transition of the $Cu^{2+}$ ions in the $4b$ subsystem. More information on absorption can be found in Refs. [20–22].

PL is observed energetically below the ZP line in absorption; see Fig. 3(b). As stated above, efficient emission is very unusual for magnetic oxides with $Cu^{2+}$ ions because we are unaware of any report on PL in such compounds. The PL spectra comprise many distinct lines of various shape and intensity in the range from 1.4052 down to 1.3 eV continued by a structureless band extending down to 1.2 eV (not shown here). Our goal in this paper is to understand the origin of the PL lines and to investigate their properties in the different magnetic phases. For that we will focus on the spectral range 1.365–1.405 eV. At $T = 5$ K, the most intense PL line is located at 1.3935 eV. It has a linewidth of 1.1 meV, identical to the exciton absorption line at 1.4052 eV. We will show below that this line can be assigned to a particular exciton line (namely, $X_2$) and the broad satellite line on its low-energy side ($M_2$ line) to the magnon-assisted recombination of the $X_2$ exciton.

PL spectra measured in the temperature range from 1.7 up to 28 K, which cover all magnetic phase transitions, are shown in Fig. 4(a). In order to avoid laser heating of the sample, the excitation power density was kept constant at the low level of $P_{exc} = 1$ mW/cm$^2$. For the line classification we marked all distinguishable emission lines by arrows and labeled them in ascending order with $U_i$, $X_i$, or $M_i$. The meaning of these labels will be explained below. The spectral positions of these lines are given in Tables I and II. The PL spectra are greatly modified by the temperature increase. While at $T = 1.7$ K 12 lines are clearly distinguishable, at $T = 25$ K only the $X_3$ and $M_3$ lines remain. With increasing temperature the PL lines vanish successively starting from higher energy ones, e.g., the

$U_1$ line disappears already at $T = 2.2$ K. In more detail we will consider that below in Fig. 6.

For a closer look at the temperature-dependent changes, we plot the PL spectra for the specific temperatures of 1.7, 7, 15 (below $T_{N1}$), and 25 K (above $T_{N1}$) in Figs. 4(b)–4(e). One can distinguish in the spectra two types of lines. One type comprises the spectrally narrow lines with widths of 0.5–2.2 meV, which have no partners. We label them as the $U_i$ lines. The other type includes the lines associated with a partner for which three sets are seen, each one consisting of a narrow line and a broad low-energy satellite. They are labeled with $X_i$ and $M_i$, respectively, and we assign them to exciton ($X_i$) emission and magnon-assisted exciton ($M_i$) emission.

### 1. Exciton and magnon-assisted exciton emission

We will focus next on the properties of the $X_i$-$M_i$ sets of PL lines. As indicated, three of them can be identified in the studied spectral range. Their relative intensities strongly depend on temperature, but not the ratio of intensities of the $X_i$ and $M_i$ lines within each set. The latter fact indicates that the $X_i$ and $M_i$ lines are closely linked to each other within the

TABLE I. PL line properties of the $X_i$-$M_i$ sets at $T = 2.5$ K. In the fourth column the PLE energies ($E_{PLE}$) for the $X_i$ lines are given. $\Delta E_{abs}$ denotes the shift of the respective line from the ZP line in absorption (ZPL$_{abs}$).

| Line | $E$ (eV) | FWHM (meV) | $E_{PLE}$ (eV) | $\Delta E_{abs}$ (meV) | $\Delta E^*$ (meV) |
|------|----------|------------|----------------|------------------------|--------------------|
| ZPL$_{abs}$ | 1.4052 | 0.8 | | 0 | - |
| $X_1$ | 1.4020 | 0.7 | 1.4027 | 3.2 | 6.6 |
| $M_1$ | 1.3954 | 3.1 | | 9.8 | |
| $X_2$ | 1.3938 | 1.3 | 1.3941 | 11.4 | 6.1 |
| $M_2$ | 1.3877 | 4.7 | | 17.5 | |
| $X_3$ | 1.3743 | 1.7 | 1.3742 | 30.9 | 6.5 |
| $M_3$ | 1.3678 | 3.7 | | 37.4 | |

TABLE II. $U_i$ line properties at $T = 2.5$ K. The data for the $U_1$ line are given for $T = 1.7$ K. $\Delta E_{abs}$ denotes the shift of the respective $U_i$ line from the ZPL line in absorption at 1.4052 eV energy. In the last column the PLE energies ($E_{PLE}$) for the $U_i$ lines are given.

| Line | $E$ (eV) | FWHM (meV) | $\Delta E_{abs}$ (meV) | $E_{PLE}$ (eV) |
|------|----------|------------|------------------------|----------------|
| $U_{abs}^{PL}$ | 1.4052 | 2.2 | 0 | 1.4052 |
| $U_1$ | 1.4032 | 1.2 | 2.0 | 1.4039 |
| $U_2$ | 1.4008 |  | 4.4 |  |
| $U_3$ | 1.3989 | 1.6 | 6.3 | 1.3996 |
| $U_4$ | 1.3975 | 1.8 | 7.7 | 1.3974 |
| $U_5$ | 1.3966 | 1.5 | 8.6 | 1.3962 |
| $U_6$ | 1.3837 | 1.3 | 21.5 | 1.3855 |
| $U_7$ | 1.3780 |  | 26.2 |  |

same set and that they may belong to the same exciton state. We attribute the $X_i$ lines to zero-phonon (and zero-magnon) emission from the different exciton states whereas the $M_i$ lines can be attributed to magnon-assisted exciton recombination. This is a plausible assumption already at this stage, but we will show below that further experimental data support well this interpretation. In order to illustrate all three sets, we show in Fig. 5 the profiles of the $X_i$-$M_i$ sets for $T = 2.5$ K where the intensities of the different sets are quite comparable. Here the background emission and the $U_i$ lines are subtracted for convenience. The spectral characteristics of the $X_i$ and $M_i$ lines are summarized in Table I.

Starting from the first ($X_1$-$M_1$) set, shown in black in Fig. 5, one notes that the $X_1$ emission line is Stokes shifted by 3.2 meV from the ZP line in absorption at 1.4052 eV (in red). For convenience, in Fig. 5 we display the energy scale both in absolute values and as Stokes shift relative to the absorption line ($\Delta E_{abs}$). The shifts of the $X_2$ (orange) and $X_3$ (purple) lines are 11.4 and 30.9 meV, respectively. The exciton $X_1$ line has a linewidth of 0.7 meV, which is close to that of the absorption line. The $X_2$ and $X_3$ lines have larger widths of 1.3 and 1.7 meV, respectively.
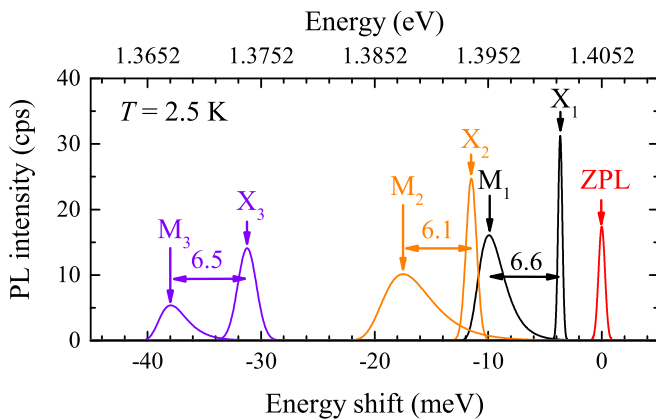


FIG. 5. Close-ups of the $X_i$-$M_i$ emission sets plotted *vs* the energy shift from the ZP absorption line (red) at 1.4052 eV. The shown lines are obtained from the PL spectrum measured at $T = 2.5$ K, by subtracting the background and the contribution of neighboring lines. The numbers above the horizontal arrows give the energy differences $\Delta E_i^*$ between $X_i$ and $M_i$ in meV.
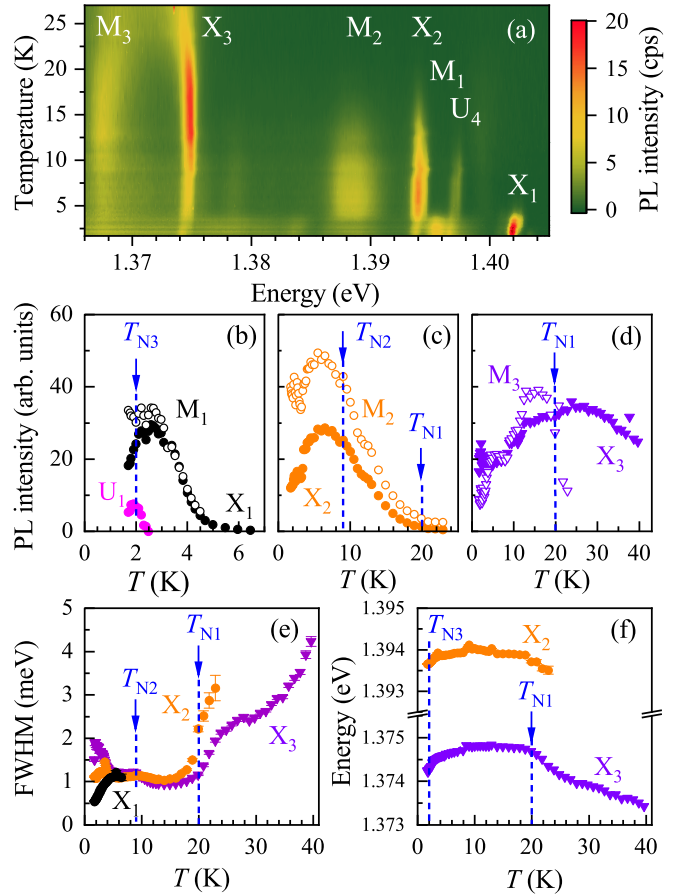


FIG. 6. (a) Contour plot of the temperature-dependent PL intensity. $E_{exc} = 1.42$ eV, $P_{exc} = 4$ mW/cm$^2$. (b–d) Temperature dependence of the exciton and exciton-magnon $X_i$-$M_i$ integral PL intensities in the (b) low ($< 7$ K), (c) medium ($< 25$ K), and (d) high ($< 42$ K) temperature range. The results pertain to the $X_i$-$M_i$ lines depicted in Fig. 4. (e) FWHM and (f) peak energy of the exciton lines as function of temperature. The magnetic phase transition temperatures ($T_{N1} = 20$ K, $T_{N2} = 9$ K, and $T_{N3} = 2$ K) in CuB$_2$O$_4$ are shown by the vertical dashed lines. The error bars do not exceed the symbol size.

We suggest that the considered $X_i$ lines are Frenkel excitons at the Cu$^{2+}$ ion sites of the $4b$ subsystem. This gives rise to several questions about their properties that can be formulated as follows:

(i) What is the origin of their shift from the absorption line? Can all of them be considered as phonon-assisted or magnon-assisted satellites of the very same exciton state at 1.4052 eV? Can the shift be related to a configuration shift or is the shift related to impurities or defects?

(ii) The $X_i$-$M_i$ emission intensity depends strongly on temperature and has clear correlation with the magnetic phases. Are specific $X_i$ states stable only in specific magnetic phases? Alternatively, one could suggest that the $X_i$ states are present at all temperatures (in all phases), but the energy relaxation between them is strongly controlled by temperature and/or magnetic ordering, determining the state population and, therefore, the relative PL intensities.

(iii) What are the population channels for the $X_i$ states for nonresonant optical photogeneration with $E_{exc} > 1.4052$ eV?

(iv) What controls the linewidth of the $X_i$ lines, the radiative decay, the inhomogeneous broadening or the magnetic interactions? Note that the radiative broadening can be excluded, as the measured recombination times are very long, corresponding to homogeneous widths smaller than a $\mu$eV; see Sec. IV D.

From results of our studies we can address at least some of these questions. In the following we discuss changes in PL spectra with increasing temperature. In addition to Fig. 4, we present them as a three-dimensional contour plot in Fig. 6(a). One can clearly see here that the intensities of the different $X_i$-$M_i$ sets increase and decrease in specific temperature ranges, which are well correlated with the different magnetic phases. The integral PL intensities of the $X_1$, $X_2$, and $X_3$ lines are shown in Figs. 6(b)–6(d) as a function of temperature. The $X_1$ intensity increases by 30% from 1.7 to 2.5 K and then decreases and diminishes above 7 K [Fig. 6(b)]. The $X_2$ line triples its intensity up to 7 K, where it has a maximum. For further temperature increase its intensity decreases and the line disappears at 23 K, i.e., slightly above $T_{N1}$ [Fig. 6(c)]. In turn, the $X_3$ intensity reaches a maximum at 23 K and stays significant even for temperatures above 40 K [Fig. 6(d)]. The temperatures at which the maximal intensities are approached and at which the PL lines disappear are in close agreement with the phase transition temperatures: $T_{N3} \approx 2$ K, $T_{N2} = 9$ K, and $T_{N1} = 20$ K. Furthermore, one notes a kind of cascaded behavior between the $X_i$ lines: the temperatures at which the $X_1$ ($X_2$) line disappears correspond to the maximal intensity of the $X_2$ ($X_3$) lines, respectively. The difference in these temperatures does not correspond to the energy splitting between the states, so that the behavior cannot be assigned to thermal dissociation. We discuss below whether it can be explained by a successive energy transfer between these states, for which the results of time-resolved experiments will be considered. One can see in Figs. 6(b)–6(d), that the $M_i$ line intensities follow with good agreement the temperature dependencies of the $X_i$ lines.

The linewidths of the $X_i$ lines also have a remarkable correlation with the magnetic phases; see Fig. 6(e). We observe that the widths of the $X_2$ and $X_3$ line remain constant at about 1.1 meV in the temperature range from 5 to 20 K, where the $X_1$ line is already gone. Their widths strongly increase above 20 K, where $CuB_2O_4$ exhibits the transition to the paramagnetic phase. In this phase, the width of the $X_2$ line reaches 3.1 meV at 23 K, and the $X_3$ line reaches 4.5 meV at 41 K. At temperatures above 41 K the $X_3$ line strongly broadens which complicates its evaluation. Below 5 K, the linewidth of $X_i$ undergoes a different change. While the $X_2$ linewidth stays about constant for a temperature decrease down to 1.7 K, the width of $X_1$ decreases down to 0.5 meV. The width of $X_3$ increases up to 1.8 meV. These characteristics indicate that a considerable part of the linewidth is controlled by exchange interactions within the system of magnetic $Cu^{2+}$ ions. Comparing the data at $T = 1.7$ K, we suggest that the inhomogeneous broadening of the $X_i$ lines does not exceed 0.5 meV, which is the smallest width of the $X_1$ line. Thus, one can conclude that the FWHM temperature dependencies of all $X_i$ lines are provided by the exchange interactions, which in turn are controlled by the magnetic phases.
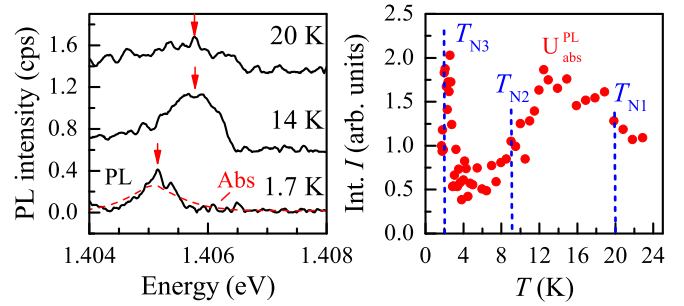


FIG. 7. (a) PL spectra in the energy range from 1.404 to 1.408 eV for different temperatures, $E_{exc} = 1.42$ eV, $P_{exc} = 4$ mW/cm$^2$. The absorption spectrum at $T = 1.7$ K is shown by the dashed red line. The maxima of the absorption for different temperatures are highlighted by the vertical red arrows. The $U_{abs}^{PL}$ emission peak is attributed to the direct exciton recombination of the light absorbed at the ZP line at 1.4052 eV. (b) Integral intensity of the $U_{abs}^{PL}$ line normalized to the value at 1.7 K as a function of temperature. Phase transition temperatures are highlighted by vertical dashed lines. The error does not exceed the symbol size.

The peak energy of the exciton lines changes little in the investigated temperature range; see Fig. 6(f). With increasing temperature from 1.7 to 2.2 K the $X_i$ lines shift weakly (by about 0.6 meV) to higher energies. Then their peak energies remain constant up to 20 K. For $T > 20$ K, they shift to lower energies. The shifts of the $X_2$ and $X_3$ lines are very similar to each other. Note that they follow well the shift of the absorption line at 1.4052 eV reported in Ref. [52].

### 2. $U_{abs}^{PL}$ emission line

We briefly address the properties of the $U_{abs}^{PL}$ emission line, which has no Stokes shift from the zero phonon absorption line at 1.4052 eV. One can clearly see in Fig. 7(a) that their spectral positions and linewidths coincide at $T = 1.7$ K. With increasing temperature the $U_{abs}^{PL}$ line broadens. It is no longer detectable above 22 K. This can be attributed to the fact that the integral intensity of this line is very small, namely two orders of magnitude weaker than the $X_2$ line.

The integral PL intensity of $U_{abs}^{PL}$ has a highly nonmonotonic temperature dependence; see Fig. 7(b). It increases twofold with increasing temperature from 1.7 K to 2.2 K and then drops below its initial value at 3.5 K. It is reasonable to relate these changes to the magnetic phase transition at $T_{N3} \approx 2$ K to which the PL intensity is obviously sensitive. However, the underlying mechanism requires further investigations. Note that, with further increasing temperature, the PL intensity reveals a second maximum at about 16 K.

### 3. $U_1$ emission line

The $U_1$ emission line is located at 1.4032 eV and has the smallest Stokes shift of 2 meV from the absorption line. It has also the smallest linewidth of 1.2 meV among all $U_i$ lines; see Table II. Starting from 1.7 K, with increasing temperature its intensity increases by 55%, reaching a maximum at 1.9 K, and then decreasing until disappearance at 2.2 K; see Fig. 6(b). Therefore, its intensity is closely correlated with the phase transition at $T_{N3} \approx 2$ K. From the spectra we cannot identify

the magnon-assisted satellite corresponding to the $U_1$ line. As the $U_1$ intensity is rather weak (five times smaller than that of the $X_1$ line at $T = 1.7$ K), the satellite could be also simply too weak to be distinguished in the spectra due to overlap with the $M_1$ and $U_5$ lines.

## B. Photoluminescence excitation spectroscopy

Photoluminescence excitation (PLE) spectroscopy is a powerful method to investigate the electronic structure of specific emission centers, including their excited states, as well as the transfer of excitation between states. It is complementary to absorption measurements, from which all states contributing to light absorption can be determined. The PLE spectroscopy has the advantage of excitation and detection selectivity, because the signal is detected at a specific emission line (or in a specific spectral energy), while the photon energy of the exciting laser is tuned. The intensity of the lines resolved in the PLE spectrum is not only given by the light absorption at the specific excited states, but also by the efficiency of energy relaxation of photoexcited carriers or excitons to the state where the signal is detected. Using the PLE spectroscopy, our goal is to obtain information about the excited states of the excitons resulting in the $X_i$ lines, the interaction between the $X_i$ states, and the origin of the $U_i$ lines.

The measured PLE spectra of $CuB_2O_4$ at $T = 1.7$ K are shown in Fig. 8 where in panel (a) the PL and absorption spectra are presented for convenient comparison. In Fig. 8(b) the PLE spectra detected at the $X_2$ (red) and $M_2$ (green) lines are shown. As expected, the strongest line in the PLE spectra is found at the photon energy of 1.4052 eV corresponding exactly to the zero-phonon exciton absorption in the 4*b* subsystem; see the open symbols in Figs. 8(b) and 8(c). In the spectral range from 1.393 to 1.404 eV, four PLE lines are clearly distinguishable. However, their intensities are about 20 times weaker than that of the main 1.4052 eV line. This important result demonstrates that the PL spectrum cannot be explained only by phonon-assisted and magnon-assisted recombination of exciton states at 1.4052 eV, but the emission from real electronic states has to be considered as well. For the $M_2$ line detection (at 1.3877 eV), PLE lines are found in close vicinity of the $X_2$, $U_4$, $U_3$, and $X_1$ lines. All of them are slightly shifted to higher energies by about 0.4 meV from the corresponding emission lines; see Tables I and II. For the $X_2$ line detection (at 1.3936 eV) three lines are observed (namely $U_4$, $U_3$, and $X_1$). The $X_2$ line overlaps with the detection energy, therefore, it cannot be resolved. The observation of the $X_1$ signal in the PLE spectrum while detecting at $X_2$ indicates that there is an energy transfer between the $X_1$ and $X_2$ states. We will comment on this later in this paper.

The PLE spectrum detected at the $X_3$ line (1.3743 eV), shown in Fig. 8(c), differs considerably from the PLE spectra measured at the $X_2$ and $M_2$ lines; compare with Fig. 8(b). The only common feature is the presence of the strong line at 1.4052 eV. By setting the detection to the $X_3$ line, in the lower energy range only a signal in close vicinity of $U_5$ is seen. This feature is absent in the PLE spectrum whilst detecting on $X_2$ ($M_2$). The fact that no lines corresponding to $X_1$ or $X_2$ light absorption are detected for $X_3$ PLE, means that a direct
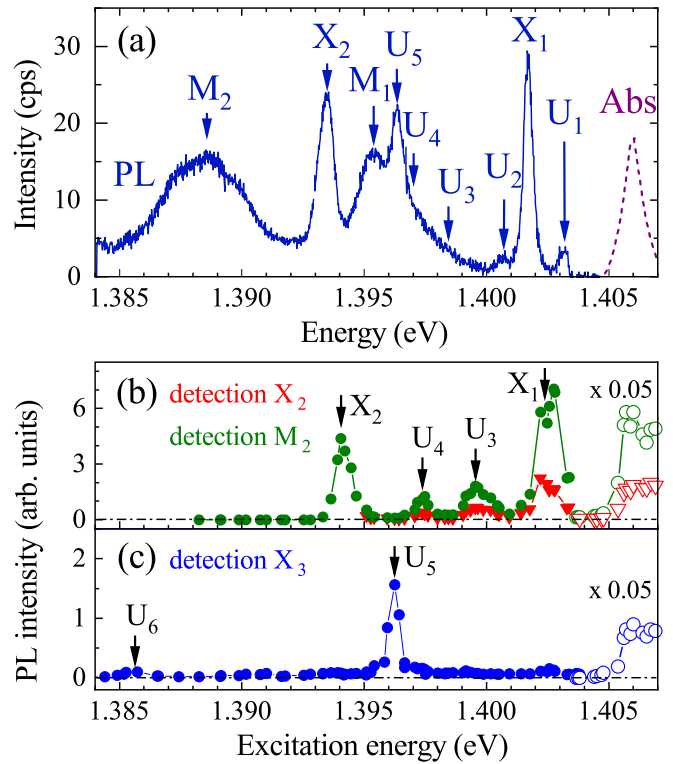


FIG. 8. (a) PL spectrum (blue line) measured for nonresonant excitation at 1.42 eV, $T = 1.7$ K. The absorption spectrum is shown by the violet dashed line. (b) PLE spectra detected at the position of the $X_2$ line (1.3936 eV, red triangles) and $M_2$ line (1.3877 eV, green circles). (c) PLE spectrum detected at the $X_3$ line (1.3743 eV), $P_{exc} = 10$ mW/cm$^2$. For the sake of visualization of weaker features in (b) and (c), the strong integral intensities above 1.403 eV are multiplied by a factor of 0.05 (open symbols).

transfer from the $X_1$ or $X_2$ states to the $X_3$ state is totally or at least strongly suppressed.

In the spectral range of the $M_1$ and $M_2$ lines, no corresponding lines are found in the PLE spectra. This is in line with our assignment of these lines to magnon-assisted recombination of the associated exciton states as in this case no light absorption is expected at energies lower that the $X_i$ line energies. In principle, magnon-assisted absorption can be detected on the high-energy sides of the exciton lines, however its intensity is very small and, therefore, not easy to observe experimentally. It is worthwhile to mention that we also found weak lines corresponding to $U_5$, $U_6$ and $X_3$ by detecting on $M_3$ in the PLE spectra (not shown here).

In Fig. 9 we show PLE spectra measured at $T = 6$ K, i.e., above the phase transition $T_{N3} \approx 2$ K. One can see that these spectra are very similar to the results measured below the transition at $T = 1.7$ K; compare to Figs. 8(b) and 8(c). All states related to the respective detection energies are well seen at both temperatures. From that we conclude that the transfer pathways are not influenced by the phase transition at $T_{N3} \approx 2$ K. We will use this conclusion for the consideration of the population and relaxation scenario of the $X_i$ states presented in Sec. V.

The observation of absorption lines associated with the $X_i$ states in the PLE spectrum is very important for the
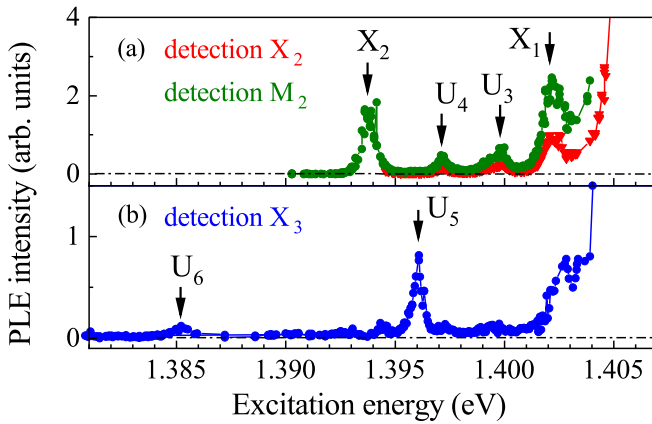
FIG. 9. PLE spectra measured at $T = 6$ K. (a) Spectra detected at $X_2$ line (1.3937 eV, red triangles) and $M_2$ line (1.3876 eV, green circles), $P_{exc} = 10$ mW/cm$^2$. (b) PLE spectrum detected at $X_3$ line (1.3743 eV).

interpretation of the origin of Frenkel exciton states. The experimental occurrence of the $X_i$ lines in CuB$_2$O$_4$ in combination with their properties is similar to observations made for Mn$^{2+}$-ion luminescence in the antiferromagnet MnF$_2$ [64]. In this study, impurity-induced modifications of the PL spectra were observed and explained by means of emission from Mn$^{2+}$ ions, which are perturbed by nearby impurity ions. The energy levels of the perturbed Mn$^{2+}$ ion can be shifted to lower energies and thus create a trap for freely propagating intrinsic excitons. Despite the very small concentration of perturbed ions, their PL at low temperatures is reported to be much stronger than the one of the free excitons, as free excitons become localized on them. Note that the role of the impurity in this case is very different from what one would commonly expect in semiconductor physics, as the electronic states of the impurities are not involved in the emission. The impurity role is limited to the shift of the Mn$^{2+}$-ion energy levels. The three $X_i$ states observed in CuB$_2$O$_4$ can either be related to three types of impurities or to the Cu$^{2+}$ ions in the 4$b$ subsystem whose local coordination (the crystal-field strength) is slightly perturbed by remote impurities.

Note that the studied CuB$_2$O$_4$ samples are not intentionally doped and we do not have information on the impurity type and concentration level. We have examined crystals grown by two different methods and did not notice any significant difference in their optical properties (optical absorption and emission). We may suppose that some kind of intrinsic defects can be present in the crystals, e.g., such as oxygen vacancies and/or Cu$^{1+}$, Cu$^{3+}$ copper ions. Future experiments with specially doped CuB$_2$O$_4$ samples may help to clarify the role of impurities and defects in the emission spectra.

### C. PL spectra under selective excitation

It is instructive to analyze PL spectra measured under selective excitation at specific resonances that were identified in the PLE spectra. In Fig. 10 we show four of such spectra excited through the $X_1$, $U_3$, $U_5$, and $X_2$ resonances.

For selective excitation of $X_1$ ($E_{exc} = 1.4027$ eV), luminescence from all lower in energy lines is observed; see
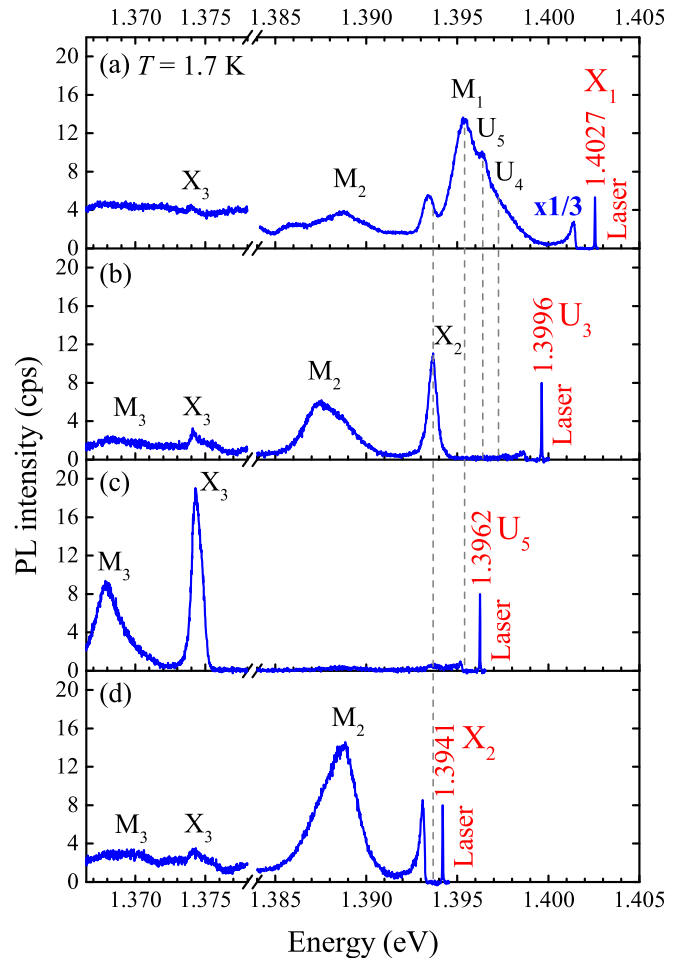


FIG. 10. PL spectra for resonant excitation of the (a) $X_1$, (b) $U_3$, (c) $U_5$, and (d) $X_2$ states, $T = 1.7$ K, $P_{exc} = 10$ mW/cm$^2$. Note that for better visibility the spectral range between 1.378 and 1.384 eV is left out. The intensity in spectrum (a) is scaled by a factor of 0.3. The PL peak positions are indicated by the dashed lines. The laser line marked in each spectrum was measured with a strong neutral filter in the detection path. The laser energy for each spectrum is given by the red numbers in eV.

Fig. 10(a). The spectrum is similar to the one measured for nonresonant excitation [see Fig. 4(b)] with $M_1$ being the most intense line. However, the lines $X_3$ and $M_3$ are less pronounced for selective excitation of $X_1$. This indicates that there is no direct transfer between $X_1$ and $X_3$ states.

When the excitation energy is tuned in resonance with the $U_3$ absorption ($E_{exc} = 1.3996$ eV), the $X_2$ and $M_2$ lines are the most intense components in the spectrum [Fig. 10(b)]. This observation provides evidence that the $U_3$ and $X_2$ states are coupled. The PL signal in the range of $X_3$ and $M_3$ lines is particularly weak. The same applies if $X_2$ is excited selectively ($E_{exc} = 1.3941$ eV); see Fig. 10(d). Here mainly the $M_2$ line can be observed. These findings are in agreement with our conclusion from the PLE spectra that the exciton transfer from the $X_2$ to the $X_3$ state is suppressed.

For selective excitation of the $U_5$ state ($E_{exc} = 1.3962$ eV), only the $X_3$ and $M_3$ lines are observed [Fig. 10(c)], despite the fact that the $U_5$ state has a higher energy than the $X_2$ state.
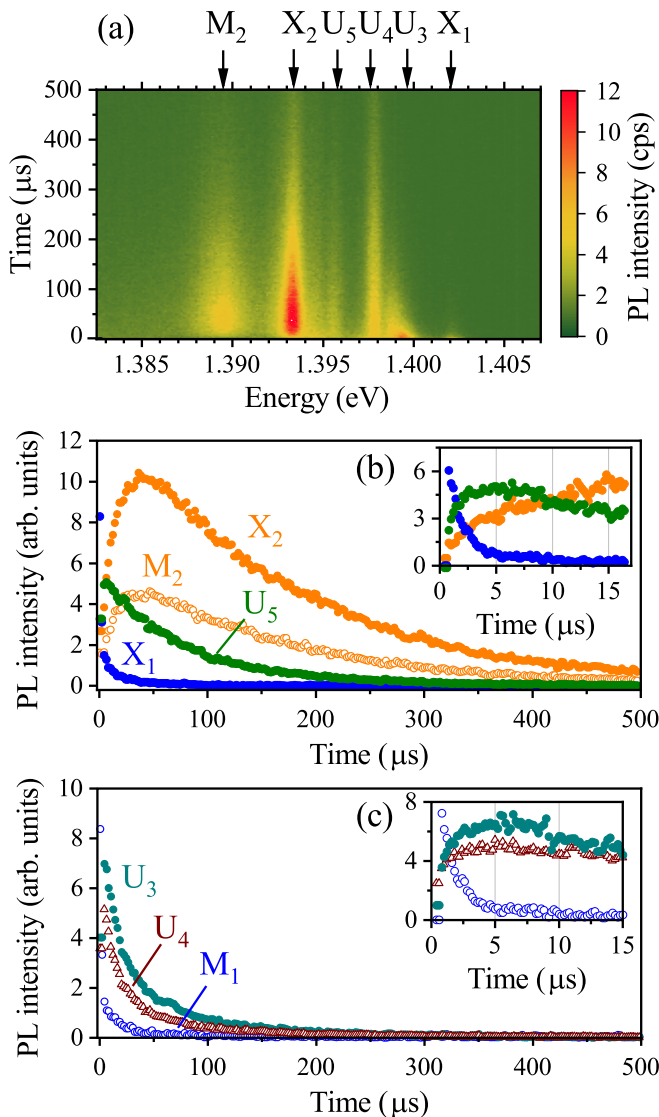
FIG. 11. (a) Contour plot of the time-resolved PL intensity. $T = 5$ K, $P_{exc} = 7$ mW/cm$^2$, $E_{exc} = 2.33$ eV. (b–c) Temporal evolution of the integrated PL intensity of the different PL lines. The dynamics in the time range of up to 17 $\mu$s are enlarged in the insets.

Therefore, we conclude that the $U_5$ state does couple with $X_3$ but has no interaction with $X_2$.

It is worth noting that the shape of the $M_2$ line depends on the excitation conditions; compare Figs. 10(a), 10(b), and 10(d) for different selective excitations and Fig. 8(a) for nonresonant excitation. The linewidth remains about the same in the range of 2.7–4.7 meV, but the asymmetry shape as well as the maximal shift from the $X_2$ line vary. A rather symmetric line is observed for nonresonant excitation. As soon as the excitation is tuned in resonance with the $X_1$ and $X_2$ states, the line shape of $M_2$ becomes asymmetric with the maximum on the high-energy side (shift of 5.0 meV); see Figs. 10(a) and 10(d). For selective excitation of the $U_3$ state, on the other hand, the maximum shifts to the low-energy side (shift of 6.2 meV); see Fig. 10(b). A detailed analysis of the shape of the magnon-assisted exciton emission lines is beyond the scope of this paper.

TABLE III. Rise and decay times of emission lines. $T = 5$ K, $P_{exc} = 7$ mW/cm$^2$. The $X_2$-$M_2$ set shows a biexponential rise dynamics; see inset in Fig. 11(b). The rise time of the $X_3$-$M_3$ set could not be measured.

| Peak | $\tau_{r1}$ ($\mu$s) | $\tau_{r2}$ ($\mu$s) | $\tau_d$ ($\mu$s) |
|---|---|---|---|
| $X_1$ | <0.005 | | 1.4 |
| $M_1$ | <0.005 | | 1.8 |
| $U_5$ | 0.02 ± 0.01 | | 120 |
| $U_3$ | 1.3 | | 16 |
| $U_4$ | 1.2 | | 10 |
| $X_2$ | 1.4 | 11 | 140 |
| $M_2$ | 1.6 | 12 | 140 |
| $X_3$ | | | 190 |
| $M_3$ | | | 190 |

**D. Time-resolved photoluminescence**

Further insight into the origin of the emission lines and the coupling between the states can be obtained by time-resolved measurements of the recombination dynamics. In Fig. 11(a) an overview of the time-resolved PL spectra after pulsed nonresonant excitation ($E_{exc} = 2.33$ eV) is shown for $T = 5$ K. The repetition period of the laser was set to 10 s in order to give the system sufficient time to return to the ground state. From the time evolution of the PL spectrum we conclude that all lines in the spectrum have their own relaxation decay times and these times increase towards lower energy. Thus, we monitor a cascaded decay of the PL lines with the lines at higher energy fading away first. Their spectral position and linewidth do not change with increasing time.

The emission dynamics of the $X_1$, $U_5$, $X_2$, and $M_2$ lines as well as those from the $U_3$, $U_4$, and $M_1$ lines are highlighted in Figs. 11(b) and 11(c), respectively. The involved time scales are summarized in Table III. In the following, we discuss the details important for interpretation given at the end of this section together with the temperature dependence of the rise and decay times. From the experimental data we can determine a rise ($\tau_r$) and decay ($\tau_d$) time for each feature. The initial rise time can be either very short (< 5 ns) for the $X_1$, $M_1$ and $U_5$ lines, or quite long in the range of 1–12 $\mu$s for $X_2$, $M_2$, $U_3$, and $U_4$ lines. In the special case of $X_2$ and $M_2$, two characteristic rise times can be derived from the increase of PL intensity over time; see the inset in Fig. 11(b). The decay times ($\tau_d$) differ considerably from 1.4–1.8 $\mu$s ($X_1$, $M_1$) to 10–16 $\mu$s ($U_3$, $U_4$) and further to 120–190 $\mu$s ($U_5$, $X_2$, $M_2$, $X_3$, $M_3$). The PL lines lower in energy than $M_3$ could not be investigated in the time-resolved measurements due to their low integral intensity.

It is worth to remind that in a system with coupled electronic states, many of which contribute to the emission from CuB$_2$O$_4$, the interpretation of the emission dynamics can become highly nontrivial. Several factors need to be taken into account: (i) Decay can be provided either by radiative and nonradiative recombination or carrier depletion, e.g., relaxation to states which are lower in energy. (ii) In the time-resolved dynamics the rise and decay times of PL intensity reflect the time for a particular energy level to be populated and subsequently depopulated. The rise time
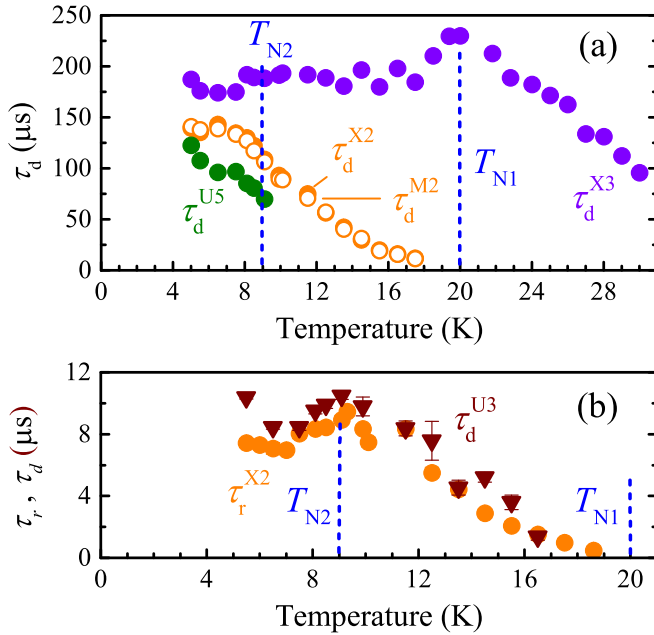
FIG. 12. (a) Temperature dependencies of decay times of various emission lines. (b) Comparison of temperature dependence of the $U_3$ decay and the $X_2$ rise dynamics. The results were measured at $P_{exc} = 7$ mW/cm$^2$ for nonresonant excitation at $E_{exc} = 2.33$ eV. The experimental errors are within the symbol size.

usually corresponds to the shortest process in population and relaxation, whereas the decay time reflects the longest of these processes. However, not always population occurs faster than the relaxation. (iii) A correlation between decay and rise times appears for states which are linked by a cascaded behavior. Then the coupling mechanisms and interaction strengths are important. (iv) The population dynamics are controlled not only by the interaction between donor and acceptor states, but also by the lifetime of the donor state itself. If the latter is shorter than the transfer time, the population dynamics reflect the relaxation time of the donor state.

One can see in Fig. 11(b) and Table III that in CuB$_2$O$_4$ rise and decay times of pairs of PL lines coincide with each other, hinting at a coupling between these states. For instance, the $X_1$ decay time corresponds to the rise time of the $X_2$ line (1.4 $\mu$s). And the $U_3$ and $U_4$ decay times (10–16 $\mu$s) coincide with the slower rise component of the $X_2$ line (11 $\mu$s).

For developing a basic understanding of the coupling between the different states and distinguish the influence of magnetic phase transitions on the dynamics, we focus next on the temperature dependence of the rise and decay times. In general one observes a shortening of $\tau_r$ and $\tau_d$ with increasing temperature; see Fig. 12. Here again clear correspondences to the magnetic phases and to the PL intensity behavior shown in Figs. 6(b) and 6(c) can be found. For instance, the $X_3$ decay time stays constant at 190 $\mu$s in the temperature range 3–17 K, then slightly increases to 225 $\mu$s at 20 K and thereafter linearly decreases to 90 $\mu$s at 30 K; see Fig. 12(a). The decay time of $X_2$ and $M_2$ is 140 $\mu$s for $T < 8$ K and decreases to 10 $\mu$s at 17 K. The $U_5$ decay time decreases from 120 $\mu$s at 5 K down to 70 $\mu$s at 9 K, finally vanishing above 9 K. The

temperature dependencies of the $U_3$ decay and $X_2$ rise times shown in Fig. 12(b) confirm that these states are coupled and that exciton relaxation between them takes place.

From the time-resolved results we draw several important conclusions:

(i) One is the confirmation of the origin of the $M_i$ lines in magnon-assisted recombination of the $X_i$ excitons. One can see from Table III that the $X_i$ and $M_i$ rise and decay times are identical and that they have the same temperature dependencies, as exemplified for the $X_2$ and $M_2$ lines in Fig. 12(a). Their decays can be related to the relaxation of $X_i$ exciton states having several relaxation options one of which is the magnon-assisted recombination.

(ii) We observe fast population dynamics of the $X_1$ (< 5 ns) and $U_5$ (< 20 ns) states by nonresonantly photogenerated excitons. Therefore, we conclude that the $X_1$ and $U_5$ states are populated by direct capture of free excitons, i.e., without involving intermediate states.

(iii) The $X_1$ decay time of 1.4 $\mu$s corresponds well to the rise time of the $X_2$, $U_3$, and $U_4$ lines. This means that the latter states are populated via the $X_1$ state, and, therefore, the $X_1$ lifetime is not controlled by radiative recombination, but rather by relaxation to lower lying states.

(iv) The observation that the decay times of $U_3$ and $U_4$ lines (10–16 $\mu$s) coincide with the second rise time of the $X_2$ line indicates that the $U_3$ and $U_4$ states serve as intermediate levels for population of the $X_2$ state, so that the lifetimes of the $U_3$ and $U_4$ states are limited by the relaxation to $X_2$. This is confirmed by the results in Fig. 12(b).

(v) The long-lasting decays of the $X_2$ (140 $\mu$s) and $X_3$ (190 $\mu$s) states at $T = 5$ K are most probably controlled by the radiative recombination of Frenkel excitons at the Cu$^{2+}$ ions. This radiative recombination is slightly accelerated by the magnon-assisted recombination resulting in the $M_i$ lines. These times are sensitive to the magnetic phase, as the $X_2$ decay shortens for $T > T_{N2}$ and the $X_3$ decay shortens for $T > T_{N1}$; see Fig. 12(a). However, the underlying mechanisms could not be clarified so far.

(vi) Lastly, the $U_5$ decay time of 120 $\mu$s is contributed by radiative recombination and relaxation to the $X_3$ state, which is confirmed by the PLE spectrum in Fig. 8(c) and PL spectrum in Fig. 10(c).

These conclusions are summarized below in Fig. 15, where we schematically represent relaxation between the states contributing to the emission of CuB$_2$O$_4$.

### E. Magnon-assisted exciton recombination

As we have discussed in Sec. II D, the magnon-assisted exciton recombination of Cu$^{2+}$ Frenkel excitons in CuB$_2$O$_4$ resulting in a broad line is governed by the width of the magnon dispersion of 2.6–7.9 meV within the Brillouin zone. These lines in the PL spectra, which are labeled by $M_i$, are shifted to lower energies from the exciton line; see also Fig. 2. Indeed, these lines are observed in the three $X_i$-$M_i$ sets. One can see in Fig. 5 that at $T = 2.5$ K for nonresonant excitation all $M_i$ lines have an asymmetric shape with their maxima shifted by about 6.1–6.6 meV from their respective exciton line. These values correspond to the magnon energies in the vicinity of the Brillouin zone boundary.
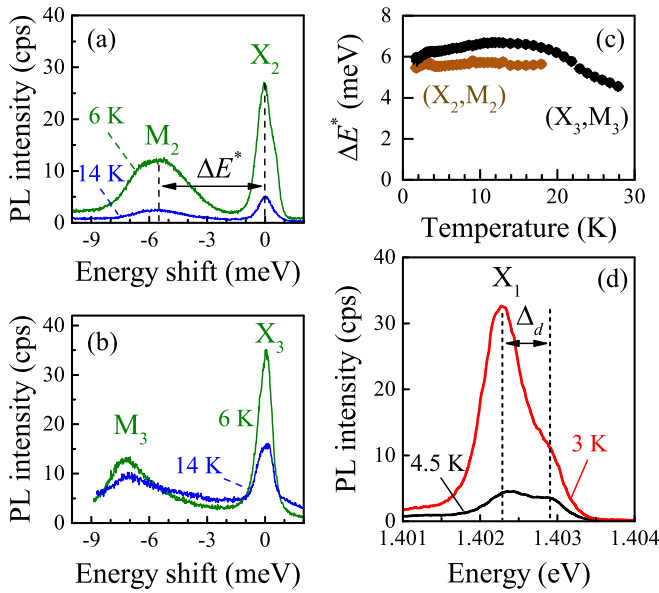
FIG. 13. PL spectra of the exciton and magnon-assisted exciton recombination for the $X_2$-$M_2$ set [(a) 1.385–1.395 eV] and the $X_3$-$M_3$ set [(b) 1.374–1.364 eV] as a function of energy shift from the respective $X_i$ line. The spectra are taken at $T = 6$ and 14 K for nonresonant excitation at $E_{exc} = 1.42$ eV with a power density of $P_{exc} = 1$ mW/cm$^2$. (c) Temperature dependence of the $M$-line shift ($\Delta E^*$). (d) PL spectrum of the $X_1$ line at $T = 3$ and 4.5 K. The Davydov splitting $\Delta_d$ is highlighted by the arrow and vertical dashed lines. The laser excitation energy and power density are the same as in (a) and (b).

It became clear that the experimental appearance of the $M_i$ lines in PLE spectroscopy is rich, it can vary and even have a symmetric shape, as shown for the $M_2$ line at $T = 1.7$ K in Fig. 8(a). Moreover, the shift of the maximum is sensitive to the photon energy of selective excitation; see Fig. 10. This change of the shape is accompanied by a shift of the magnon line maximum closer to the exciton line. A summary of this behavior is presented at the end of Sec. IV C.

To provide a comparison between the different $X_i$-$M_i$ sets at higher temperatures, in Figs. 13(a) and 13(b) we show data for the $X_2$-$M_2$ and $X_3$-$M_3$ sets measured at $T = 6$ and 14 K. For easier comparison, the energy scale is given as shift from the respective $X_i$ lines. Here the energy difference between the $X_i$ and $M_i$ maxima is denoted as $\Delta E^*$, later referred to as the $M$-line shift. Despite the same excitation conditions one sees that the $M_i$ lines differ in shape and energy shift. While the $M_2$ line is rather broad and about symmetric, the $M_3$ line is asymmetric with a larger shift of the maximum (7.2 meV). The line shapes of the $M_i$ lines do not change considerably in this temperature range, as confirmed by the temperature dependence of the $M$-line shifts in Fig. 13(c). The shifts of the line maxima are about constant in the range of 1.7–18 K. For the temperature increase above the antiferromagnetic transition at $T_{N1} = 20$ K to 28 K the $M_3$ line shift reduces from 7.1 down to 4.7 meV.

It is important to note that the exciton emission can be detected at high temperature ($\approx 45$ K), whereas the $M$-line emission can be traced only up to 30 K, as its linewidth

strongly increases. Evidently this may be related to the $T_{N1} = 20$ K phase transition from the antiferromagnetic to the paramagnetic phase, where collective spin waves cannot form anymore so that also magnons as elementary quanta of these spin waves cannot be excited. Nevertheless, in the paramagnetic phase, the so-called paramagnons can still survive and their properties are softened, being controlled by the short-range magnetic interactions between the neighboring magnetic ions.

### F. Davydov exciton splitting

The width of the energy dispersion of Frenkel excitons is controlled by the energy transfer between ions in adjacent unit cells. The interaction of ions within the same unit cell induces a splitting of the exciton states known as Davydov splitting [65]. In CuB$_2$O$_4$ the presence of two crystallographically equivalent Cu$^{2+}$ ions in the primitive cell of the $4b$ subsystem should lead to Davydov exciton doublets which depend on the magnetic structure [57]. The Davydov splitting $\Delta_d = 0.5$ meV of the lowest $4b$ exciton line was recently measured in absorption [52]. As one can see in Fig. 13(d), it can be also observed in the $X_1$ line of the PL spectra. At $T = 3$ K the lower doublet state is mostly populated and the higher state is seen as a weak shoulder, but at 4.5 K they are populated about equally. From these spectra we derive the Davydov splitting in CuB$_2$O$_4$ to be equal to $\Delta_d = 0.50 \pm 0.01$ meV. Note that the Davydov splitting is expected to occur for all exciton lines, i.e., it is expected also for the $X_2$ and $X_3$ lines as well. However, we have not observed it for these lines, which is most probably due to their larger linewidths.

### G. Heating of CuB$_2$O$_4$ by means of photoexcitation

We have shown in Figs. 4 and 6 that the intensities of the $X_i$ and $M_i$ lines are very sensitive to the lattice temperature, so that they could be used for thermometric measurements. In optical experiments with laser excitation one should be careful to avoid laser heating of the crystal lattice and/or the system of magnetic ions. Note that in materials with weak coupling of the magnetic system to the phonon bath, i.e., long spin-lattice relaxation, different temperatures for the magnetic ion and phonon system can be established under photoexcitation. Such phenomena have been studied in diluted magnetic semiconductors with Mn$^{2+}$ magnetic ions [66,67].

In the experiments presented in the previous sections the excitation density was kept at a very low level to ensure that optical heating is avoided. Here we show experimental spectra illustrating the effect of laser heating and discuss its consequences. In Fig. 14(a) PL spectra measured at $T = 3$ K for different excitation densities of nonresonant laser excitation varying about four orders of magnitude from 0.3 up to 350 mW/cm$^2$ are shown. Generally, the increase of excitation power density leads to a linear increase of the integral intensity of the PL spectrum calculated in the energy range from 1.392 up to 1.406 eV; see Fig. 14(b). This tells us that the used excitation densities are reasonably low and no new recombination mechanisms like bimolecular recombination or Auger processes are involved. However, we observe also a spectrum change, i.e., a change of the intensity ratios among the $X_i$, $M_i$, and $U_i$ lines. The induced changes due to increasing
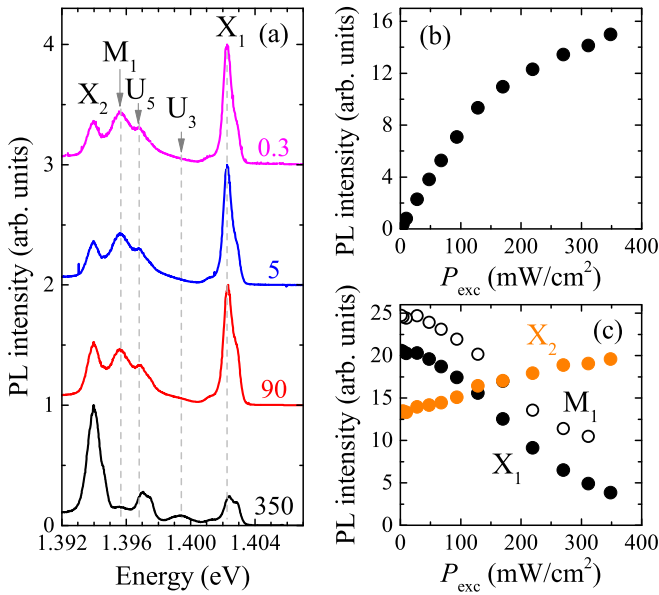
FIG. 14. (a) PL spectra measured at various laser power densities $P_{exc}$ given by the numbers in mW/cm$^2$. $T = 3$ K, $E_{exc} = 1.42$ eV. The spectra are normalized to their PL maximum. (b) Integral intensity of the PL spectrum in the energy range from 1.406 to 1.392 eV as a function of excitation power density ($P_{exc}$). (c) Excitation power dependence of the $X_1$, $M_1$, and $X_2$ integral intensities. To ensure a proper comparison at each measured power density, the respective spectrum was renormalized to the spectrum recorded at power density of 1 mW/cm$^2$ and subsequently the individual integral intensities were determined.

power density are similar to the temperature induced variations; compare with Fig. 4. Namely, the $X_1$ and $M_1$ normalized intensities decrease and the $X_2$ intensity grows, as shown in detail in Fig. 14(c). Comparing these results with Figs. 6(b) and 6(c) we evaluate the lattice temperature to be 4.5 K for an excitation density of 350 mW/cm$^2$, i.e., it has increased by 1.5 K above the bath temperature. It is worthwhile noting that also the shape of the $X_1$ line, where the Davydov splitting can be seen, agrees well with the temperature induced changes from Fig. 13(d). The results presented in this section underline that care has to be taken when experiments with pulsed laser excitation are performed on CuB$_2$O$_4$, where typically rather high excitation densities are used.

## V. SUMMARY ON OPTICAL TRANSITIONS IN CuB$_2$O$_4$

Here we summarize the results on the structure of the electronic levels contributing to the photoluminescence in CuB$_2$O$_4$ and give a scheme of the relaxation channels providing population and relaxation of the three sets of emission lines, namely $X_1$-$M_1$, $X_2$-$M_2$, and $X_3$-$M_3$. The summary is presented in Fig. 15, where in panel (a) we give an overview of the optical transitions detected in the PLE and PL spectra. Note that only the strongest in intensity PLE transition at 1.4052 eV [see Figs. 8(b) and 8(c)] was observed in absorption. In general, most of the lines in the PLE spectrum should be observed also in absorption. Exceptions can be related to phonon-assisted or magnon-assisted energy relaxation processes, which in case of samples with considerable nonradiative recombination may give additional transitions. We may
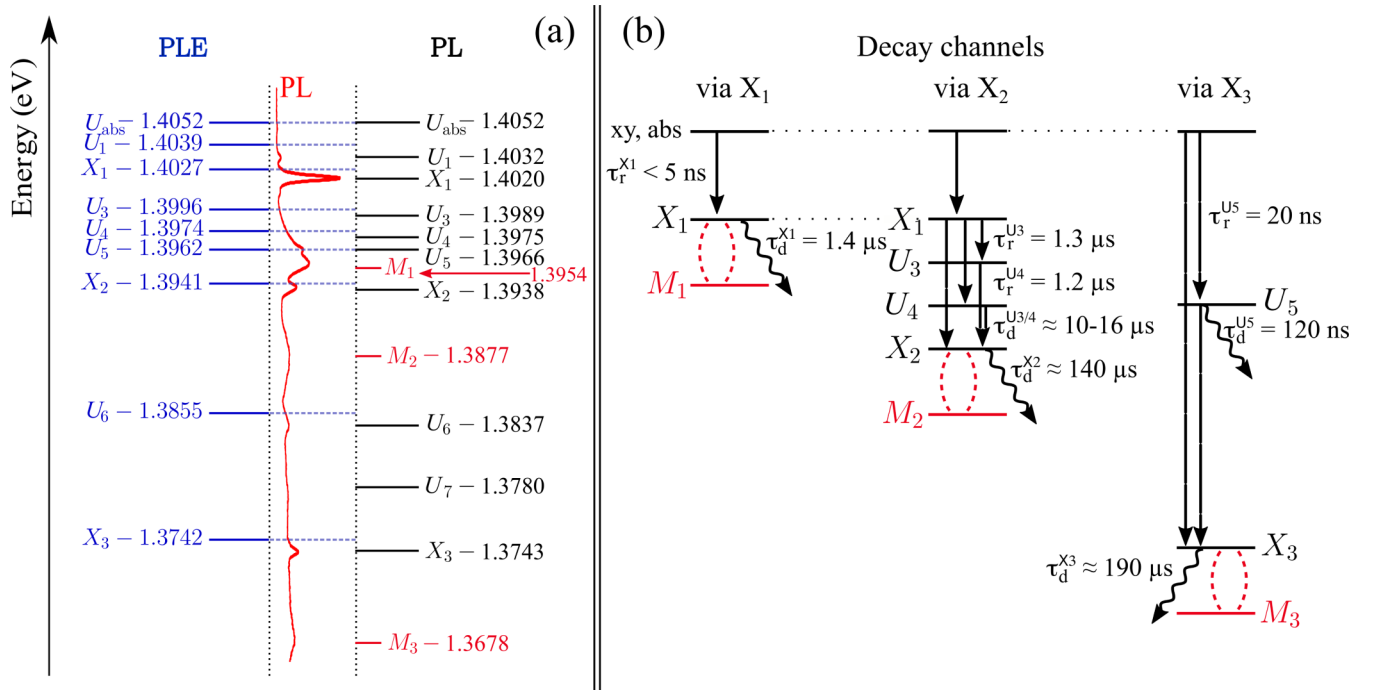


FIG. 15. (a) Schematic illustration of the energy-level scheme in PLE (blue) and PL (black) at $T = 2.5$ K. The PL spectrum at $T = 1.7$ K is shown in red. The values of each energy level are given in eV. (b) Schematics of energy levels and channels providing population and relaxation of the three $X_1M_1$, $X_2M_2$, and $X_3M_3$ exciton-magnon sets. Arrows mark processes that are established in our experiments. The determined decay or raise times are given. Transitions related to magnon-assisted exciton recombination are shown in red.

suggest that much weaker transitions below 1.4052 eV can be found also in absorption.

Most of the $X_i$ and $U_i$ lines are observed in the PL and the PLE spectra. The only exception here is the $U_7$ line. However, we want to note that lines in PLE spectra can be too weak and therefore not easily detectable. From the PL and PLE spectra we conclude that the real electronic states are associated with $X_i$ and $U_i$ lines, i.e., they do not result from phonon-assisted or magnon-assisted recombination of excitons. The $M_i$ lines are seen only in PL and do not appear in the PLE spectra. This is in line with their identification as magnon-assisted recombination of the respective $X_i$ excitons, as supported by several experimental observations presented in this paper.

In the PL spectrum, we have identified three sets of $X_i$-$M_i$ lines, each composed of the Frenkel exciton line $X_i$ and the magnon-assisted recombination line $M_i$. The relative intensities of these sets are strongly dependent on temperature, showing correlation with the magnetic phase transitions in $CuB_2O_4$. Therefore, these sets may serve as valuable tools for optical detection of the magnetic properties of $CuB_2O_4$. In Fig. 15(b) we present schematically the electronic levels that are contributing to the population and relaxation of the $X_1$, $X_2$, and $X_3$ excitons, and correspondingly to the recombination dynamics of the $X_1$-$M_1$, $X_2$-$M_2$, and $X_3$-$M_3$ sets. We show here only the transitions between states that were identified experimentally. Note that the shown relaxation paths and their times are given for experiments performed at 1.7 and 5 K. They could depend on the magnetic phase and lattice temperature, which calls for further detailed studies.

One can see that the states $X_2$ and $X_3$ have decay times of 140–190 $\mu$s, which can be attributed to the radiative recombination of excitons by direct emission and magnon-assisted recombination. Note that the decay time of the $X_1$ state of 1.4 $\mu$s is much shorter. One can suggest that recombination processes provide a smaller contribution here, but the decay is mainly controlled by energy relaxation to the $U_3$, $U_4$, and $X_2$ states.

## VI. CONCLUSIONS

$CuB_2O_4$ is a unique example for a magnetoelectric antiferromagnet which exhibits unexpectedly strong photoluminescence below the lowest absorption line at 1.4052 eV related to the electronic transition within the $Cu^{2+}$ ions of the $4b$ subsystem. To the best of our knowledge, this magnetically ordered material containing $Cu^{2+}$ ions is the first example in which such an intense photoluminescence was observed. We have performed a detailed study of the spectral and dynamical properties of the photoluminescence in the temperature range of 1.7–40 K, in which several magnetic phase transitions occur including the transition from paramagnetic to the antiferromagnetic state at $T_{N1} = 20$ K. In the complex photoluminescence spectra, we identified three sets of lines, each composed of an exciton line and a satellite of magnon-assisted exciton recombination, and showed that their properties are very sensitive to the specific magnetic phase. Some other lines were identified to be excited or intermediate states coupled with the exciton states.

[1] M. Fiebig, Revival of the magnetoelectric effect, J. Phys. D: Apl. Phys. **38**, R123 (2005).

[2] W. Eerenstein, N. D. Mathur, and J. F. Scott, Multiferroic and magnetoelectric materials, Nature (London) **442**, 759 (2006).

[3] D. I. Khomskii, Multiferroics: Different ways to combine magnetism and ferroelectricity, J. Magn. Magn. Mater. **306**, 1 (2006).

[4] S.-W. Cheong and M. Mostovoy, Multiferroics: A magnetic twist for ferroelectricity, Nat. Mater. **6**, 13 (2007).

[5] N. A. Spaldin, S.-W. Cheong, and R. Ramesh, Multiferroics: Past, present, and future, Phys. Today **63**, 38 (2010).

[6] A. P. Pyatakov and A. K. Zvezdin, Magnetoelectric and multiferroic media, Phys. Usp. **55**, 557 (2012).

[7] M. Fiebig, T. Lottermoser, D. Meier, and M. Trassin, The evolution of multiferroics, Nat. Rev. Mater. **1**, 16046 (2016).

[8] R. V. Pisarev, Crystal optics of magnetoelectrics, Ferroelectrics **162**, 191 (1994).

[9] R. V. Pisarev, Broken symmetries and optical phenomena in crystals, Ferroelectrics **183**, 39 (1996).

[10] M. Fiebig, V. V. Pavlov, and R. V. Pisarev, Second-harmonic generation as a tool for studying electronic and magnetic structures of crystals: Review, J. Opt. Soc. Am. **22**, 96 (2005).

[11] T. Arima, Magneto-electric optics in non-centrosymmetric ferromagnets, J. Phys.: Condens. Matter **20**, 434211 (2008).

[12] M. Saito, K. Taniguchi, and T.-H. Arima, Gigantic optical magnetoelectric effect in $CuB_2O_4$, J. Phys. Soc. Jpn. **77**, 013705 (2008).

[13] R. V. Pisarev, Second harmonic generation spectroscopy in magnetic and multiferroic materials, J. Luminescence **133**, 169 (2013).

[14] D. Szaller, S. Bordács, and I. Kézsmárki, Symmetry conditions for nonreciprocal light propagation in magnetic crystals, Phys. Rev. B **87**, 014421 (2013).

[15] Y. Tokura and N. Nagaosa, Nonreciprocal responses from non-centrosymmetric quantum materials, Nat. Comun. **9**, 3740 (2018).

[16] S.-W. Cheong, SOS: Symmetry-operational similarity, npj Quantum Materials **4**, 53 (2019).

[17] A. E. Petrova and A. I. Pankrats, Copper metaborate $CuB_2O_4$ phase diagrams based on the results of measuring the magnetic moment, J. Exp. Theor. Phys. **126**, 506 (2018).

[18] T. Kawamata, N. Sugawara, S. M. Haider, and T. Adachi, Thermal conductivity and magnetic phase diagram of $CuB_2O_4$, J. Phys. Soc. Jpn. **88**, 114708 (2019).

[19] M. Fiebig, I. Sänger, and R. V. Pisarev, Magnetic phase diagram of $CuB_2O_4$, J. Appl. Phys. **93**, 6960 (2003).

[20] R. V. Pisarev, I. Sänger, G. A. Petrakovskii, and M. Fiebig, Magnetic-Field Induced Second Harmonic Generation in $CuB_2O_4$, Phys. Rev. Lett. **93**, 037204 (2004).

[21] R. V. Pisarev, A. M. Kalashnikova, O. Schöps, and L. N. Bezmaternykh, Electronic transitions and genuine crystal-field parameters in copper metaborate $CuB_2O_4$, Phys. Rev. B **84**, 075160 (2011).

[22] R. V. Pisarev, K. N. Boldyrev, M. N. Popova, A. N. Smirnov, V. Y. Davydov, L. N. Bezmaternykh, M. B. Smirnov, and V. Y. Kazimirov, Lattice dynamics of piezoelectric copper metaborate $CuB_2O_4$, Phys. Rev. B **88**, 024301 (2013).

[23] V. G. Ivanov, M. V. Abrashev, N. D. Todorov, V. Tomov, R. P. Nikolova, A. P. Litvinchuk, and M. N. Iliev, Phonon and magnon Raman scattering in $CuB_2O_4$, Phys. Rev. B **88**, 094301 (2013).

[24] J. N. Hancock, G. Chabot-Couture, Y. Li, G. A. Petrakovski, K. Ishii, I. Jarrige, J. Mizuki, T. P. Devereaux, and M. Greven, Resonant inelastic x-ray scattering in electronically quasi-zero-dimensional $CuB_2O_4$, Phys. Rev. B **80**, 092509 (2009).

[25] E. N. Ovchinnikova, A. Rogalev, F. Wilhelm, K. A. Kozlovskaya, A. P. Oreshko, and V. E. Dmitrienko, X-ray natural circular dichroism in copper metaborate, J. Exp. Theor. Phys. **123**, 27 (2016).

[26] S. Toyoda, N. Abe, and T. Arima, Gigantic directional asymmetry of luminescence in multiferroic $CuB_2O_4$, Phys. Rev. B **93**, 201109(R) (2016).

[27] M. Saito, K. Ishikawa, K. Taniguchi, and T. Arima, Magnetic Control of Crystal Chirality and the Existence of a Large Magneto-Optical Dichroism Effect in $CuB_2O_4$, Phys. Rev. Lett. **101**, 117402 (2008).

[28] S. W. Lovesey and U. Staub, Calculated chiral and magneto-electric dichroic signals for copper metaborate ($CuB_2O_4$) in an applied magnetic field, J. Phys.: Condens. Matter **21**, 142201 (2009).

[29] T. Arima and M. Saito, Comment on "Calculated chiral and magneto-electric dichroic signals for copper metaborate ($CuB_2O_4$) in an applied magnetic field," J. Phys.: Condens. Matter **21**, 498001 (2009).

[30] S. W. Lovesey and U. Staub, Reply to comment on "Calculated chiral and magneto-electric dichroic signals for copper metaborate ($CuB_2O_4$) in an applied magnetic field," J. Phys.: Condens. Matter **21**, 498002 (2009).

[31] S. W. Lovesey, Zeeman spectrum, magnetic neutron diffraction pattern, and Dirac multipoles for a multiferroic material $CuB_2O_4$, Phys. Rev. B **94**, 094422 (2016).

[32] D. Bossini, K. Konishi, S. Toyoda, T. Arima, J. Yumoto, and M. Kuwata-Gonokami, Femtosecond activation of magneto-electricity, Nat. Phys. **14**, 370 (2018).

[33] K. Imasaka, R. V. Pisarev, L. N. Bezmaternykh, T. Shimura, A. M. Kalashnikova, and T. Satoh, Excitation of multiple phonon modes in copper metaborate $CuB_2O_4$ via nonresonant impulsive stimulated Raman scattering, Phys. Rev. B **98**, 054303 (2018).

[34] Y. Nii, R. Sasaki, Y. Iguchi, and Y. Onose, Microwave magnetochiral effect in the non-centrosymmetric magnet $CuB_2O_4$, J. Phys. Soc. Jpn. **86**, 024707 (2017).

[35] I. Pelant and J. Valenta, *Luminescence Spectroscopy of Semiconductors* (Oxford University Press, Oxford, 2012).

[36] M. Gaft, R. Reisfeld, and G. Panczer, *Modern Luminescence Spectroscopy of Minerals and Materials* (Springer International Publishing, Cham, 2015).

[37] I. Sänger, *Magnetic-Field-Induced Second Harmonic Generation in Semiconductors and Insulators* (Shaker Verlag, Aachen, 2006).

[38] D. Kudlacik, Absorption- und Photolumineszenzspektroskopie an $CuB_2O_4$, Master's thesis, Physics Faculty, Dortmund University, Germany, 2014.

[39] D. Kudlacik, J. Debus, R. V. Pisarev, D. R. Yakovlev, and M. Bayer, Monitoring of the magnetic phase transitions by time-resolved photoluminescence in an antiferromagnet $CuB_2O_4$, in *Spin Waves 2015: International Symposium*, edited by A. M. Kalashnikova, A. V. Kimel, V. V. Pavlov, R. V. Pisarev, A. I. Smirnov, and P. A. Usachev (Ioffe Institute, St. Petersburg, Russia, 2015), p. 52.

[40] M. Martinez-Ripoll, S. Martinez-Carrera, and S. Garcia-Blanco, The crystal structure of copper metaborate, $CuB_2O_4$, Acta Cryst. Sec. B **27**, 677 (1971).

[41] G. K. Abdullaev and K. S. Mamedov, Refined crystal structure of copper metaborate $CuB_2O_4$, J. Struct. Chem. **22**, 637 (1981).

[42] G. Nénert, L. N. Bezmaternykh, A. N. Vasiliev, and T. T. M. Palstra, Magnetic, structural, and dielectric properties of $CuB_2O_4$, Phys. Rev. B **76**, 144401 (2007).

[43] W. Depmeier, H. Schmid, and F. Haenssler, $PdB_2O_4$, the first palladium borate, Naturwissenschaften **67**, 456 (1980).

[44] M. Boehm, B. Roessli, J. Schefer, A. S. Wills, B. Ouladdiaf, E. Lelièvre-Berna, U. Staub, and G. A. Petrakovskii, Complex magnetic ground state of $CuB_2O_4$, Phys. Rev. B **68**, 024405 (2003).

[45] A. I. Pankrats, G. A. Petrakovskii, M. A. Popov, K. A. Sablina, L. A. Prozorova, S. S. Sosin, G. Szimczak, R. Szimczak, and M. Baran, New magnetic states in copper metaborate $CuB_2O_4$, J. Exp. Theor. Phys. Lett. **78**, 569 (2003).

[46] G. A. Petrakovskii, K. A. Sablina, L. V. Udod, A. I. Pankrats, D. A. Velikanov, R. Szymczak, M. Baran, and G. V. Bondarenko, Effect of Ni-substitution on magnetic phase transition in $CuB_2O_4$, J. Magn. Magn. Mater. **300**, e476 (2006).

[47] T. Fujita, Y. Fujimoto, S. Mitsudo, T. Idehara, K. Inoue, J. Kishine, Y. Kousaka, S. Yano, J. Akimitsu, and M. Motokawa, High field ESR measurements on the chiral spin system $CuB_2O_4$, J. Phys.: Conf. Series **51**, 111 (2006).

[48] T. Fujita, Y. Fujimoto, S. Mitsudo, T. Idehara, T. Saito, Y. Kousaka, S.-I. Yano, J. Akimitsu, J.-I. Kishine, K. Inoue, and M. Motokawa, Commensurate to incommensurate transition in the chiral helimagnet $CuB_2O_4$, J. Phys. Soc. Jpn. **77**, 053702 (2008).

[49] A. Pankrats, G. Petrakovskii, V. Tugarinov, K. Sablina, L. Bezmaternykh, R. Szymczak, M. Baran, B. Kundys, and A. Nabialek, Magnetic phase diagram of copper metaborate $CuB_2O_4$ in magnetic field parallel to *c*-axis, J. Magn. Magn. Mater. **300**, e388 (2006).

[50] Y. Kousaka, S. Yano, J. Kishine, Y. Yoshida, K. Inoue, K. Kikuchi, and J. Akimitsu, Chiral magnetic ordering and commensurate-to-incommensurate transition in $CuB_2O_4$, J. Phys. Soc. Jpn. **76**, 123709 (2007).

[51] G. A. Petrakovskii, A. D. Balaev, and A. M. Vorotynov, Magnetic susceptibility and magnetic-field behavior of $CuB_2O_4$ copper metaborate, Phys. Solid State **42**, 321 (2000).

[52] K. N. Boldyrev, R. V. Pisarev, L. N. Bezmaternykh, and M. N. Popova, Antiferromagnetic Dichroism in a Complex Multisublattice Magnetoelectric CuB$_2$O$_4$, Phys. Rev. Lett. **114**, 247210 (2015).

[53] V. V. Menshenin, Excitons at the center of the Brillouin zone in CuB$_2$O$_4$ magnetoelectric, J. Exp. Theor. Phys. **124**, 279 (2017).

[54] D. D. Sell, R. L. Greene, and R. M. White, Optical exciton-magnon absorption in MnF$_2$, Phys. Rev. **158**, 489 (1967).

[55] R. S. Meltzer, M. Y. Chen, D. S. McClure, and M. Lowepari, Exciton-Magnon Bound State in MnF$_2$ and the Exciton Dispersion in MnF$_2$ and RbMnF$_3$, Phys. Rev. Lett. **21**, 913 (1968).

[56] D. D. Sell, Review of magnon sideband experiments, J. Appl. Phys. **39**, 1030 (1968).

[57] R. Loudon, Theory of infra-red and optical spectra of antiferromagnets, Adv. Phys. **17**, 243 (1968).

[58] G. F. Imbusch, Luminescence from solids with high concentrations of transition metal ions, in *Luminescence of Inorganic Solids*, edited by B. D. Bartolo, V. Godberg, and D. Pacheco (Springer, Boston, 1978), pp. 155–180.

[59] Y. Tanabe, T. Moriya, and S. Sugano, Magnon-Induced Electric Dipole Transition Moment, Phys. Rev. Lett. **15**, 1023 (1965).

[60] V. V. Eremenko, Y. G. Litvinenko, N. K. Kharchenko, and V. M. Naumenko, *Magneto-optics and Spectroscopy of Antiferromagnets* (Springer, New York, 1992).

[61] S. Martynov, G. Petrakovskii, and B. Roessli, Quasi-one-dimensional excitations of copper metaborate in the commen-surate phase 10K < T < 20K, J. Magn. Magn. Mater. **269**, 106 (2004).

[62] S. Martynov, G. Petrakovskii, M. Boehm, B. Roessli, and J. Kulda, Spin-wave spectrum of copper metaborate in the incommensurate phase T < 10K, J. Magn. Magn. Mater. **299**, 75 (2006).

[63] G. A. Petrakovskii, K. A. Sablina, D. A. Velikanov, A. Vorotynov, N. V. Volkov, and A. F. Bovina, Synthesis and magnetic properties of copper metaborate single crystals, CuB$_2$O$_4$, Crystallogr. Rep. **45**, 853 (2000).

[64] R. L. Greene, D. D. Sell, R. S. Feigelson, G. F. Imbusch, and H. J. Guggenheim, Impurity-induced optical fluorescence in MnF$_2$, Phys. Rev. **171**, 600 (1968).

[65] A. S. Davydov, *Theory of Molecular Excitons* (Plenum Press, New York, 1971).

[66] D. Keller, D. R. Yakovlev, B. König, W. Ossau, T. Gruber, A. Waag, and L. W. Molenkamp, Heating of the magnetic ion system in (Zn, Mn)Se/(Zn, Be)Se semimagnetic quantum wells by means of photoexcitation, Phys. Rev. B **65**, 035313 (2001).

[67] D. R. Yakovlev and I. A. Merkulov, Spin and energy transfer between carriers, magnetic ions, and lattice, in *Introduction to the Physics of Diluted Magnetic Semiconductors*, edited by J. Kossut and J. A. Gaj, Springer Series in Materials Science Vol. 144 (Springer, Berlin, 2010), pp. 263–303.